magnetochemistry

MDPI

Article

Enhanced Magnetocaloric Effect and Single-Molecule Magnet Behavior in a Series of Sulfur-Containing Ligand-Based Ln_9 Clusters (Ln = Gd, Tb, and Dy)

Ya-Wei Geng †, Tong Guo †, Xiao-Qin Wang and Tian Han *

School of Chemistry, Xi'an Jiaotong University, Xi'an 710049, China; gengyawei2025@163.com (Y.-W.G.); 18392876170@163.com (T.G.); 16685013752@163.com (X.-Q.W.)

* Correspondence: hantian0123@xjtu.edu.cn

† These authors contributed equally to this work.

Abstract

As an important branch of lanthanide-based complexes, clusters show unique properties in magnetocaloric effect (MCE) and single-molecule magnets (SMMs) using O/N ligands, while research on heavy p-block elements (e.g., S atom) with larger atomic radii and more diffuse p valence orbitals as coordinating atoms remains relatively scarce. Herein, using the sulfur-containing ligand of 2-pyridinethiol 1-oxide (HL), we successfully synthesized a series of hourglass-like Ln_9 clusters $[Ln_9(L)_{17}(\mu_3\text{-}OH)_9(\mu_4\text{-}OH)]\cdot nH_2O$ (**1**: Ln = Gd, n = 3; **2**: Ln = Tb, n = 3; **3**: Ln = Dy, n = 1). Magnetic data analysis reveals that cluster **1** shows a significant MCE, with the entropy change ($-\Delta S_m$) reaching a maximum of 34.41 J kg^{-1} K^{-1} at 2 K under ΔH = 7 T. Cluster **3**, meanwhile, exhibits distinct frequency- and temperature-dependent behavior, indicating its SMM characteristics. Interestingly, despite possessing the highest molar mass among reported Gd_9 clusters with MCE, **1** exhibits a competitive $-\Delta S_m$ value, highlighting the critical role of sulfur-containing ligand on the structure and even exchange interactions. This work offers new insights into synthesizing high-performance MCE materials and understanding magneto-structural relationships.

Keywords: lanthanide cluster; magnetocaloric effect; single-molecule magnet; sulfur-containing ligand

check for updates

Academic Editor: Carlos J. Gómez García

Received: 31 July 2025
Revised: 16 August 2025
Accepted: 18 August 2025
Published: 22 August 2025

Citation: Geng, Y.-W.; Guo, T.; Wang, X.-Q.; Han, T. Enhanced Magnetocaloric Effect and Single-Molecule Magnet Behavior in a Series of Sulfur-Containing Ligand-Based Ln_9 Clusters (Ln = Gd, Tb, and Dy). *Magnetochemistry* **2025**, *11*, 70. https://doi.org/10.3390/magnetochemistry11090070

Copyright: © 2025 by the authors. Licensee MDPI, Basel, Switzerland. This article is an open access article distributed under the terms and conditions of the Creative Commons Attribution (CC BY) license (https://creativecommons.org/licenses/by/4.0/).

1. Introduction

From household refrigerators to space probes, refrigeration technology is deeply integrated into every facet of modern society [1]. While current ^3He gas compression technology can meet ultra-low-temperature environmental demands, it faces two long-term challenges: scarcity of ^3He resources [2] and the low efficiency of traditional vapor-compression refrigeration technology (5–10% of the theoretical Carnot cycle value) [3]. Therefore, developing alternatives to ^3He has become an urgent need to support the development of future technologies. Magnetic refrigeration [4–6] has emerged as a research focus in the cooling field due to its dual advantages of high energy efficiency and environmental friendliness. The technology's core principle relies on the magnetocaloric effect (MCE), a phenomenon where magnetic materials' temperature changes with varying magnetic fields (H), enabling cooling with 30−60% Carnot cycle efficiency while eliminating ozone-damaging emissions [7].

To achieve high magnetic entropy changes ($-\Delta S_m$), a central parameter in magnetocaloric performance, metal centers with negligible magnetic anisotropy, large spin ground state, and quenched orbital angular momentum are essential [4,8–11]. The Gd^{3+} ion, with

its isotropic $^8S_{7/2}$ ground state, exemplifies these criteria and serves as a benchmark in molecular refrigerant design [4]. Efforts to enhance $-\Delta S_m$ have primarily focused on two strategies: increasing the magnetic density and engineering weak magnetic interactions [8,12]. On the one hand, the theoretical upper limit of $-\Delta S_m$ is $R\ln(2S + 1)$ (R is the gas constant and S is the spin state), typically expressed in molar units (J mol^{-1} K^{-1}) [13]. However, experimental data are often normalized to mass units (J kg^{-1} K^{-1}) or volume units (mJ cm^{-3} K^{-1}), where higher magnetic density directly correlates with larger $-\Delta S_m$. Thus, most current high-performance molecular-based magnetic refrigerants employ light ligands such as inorganic anions [14] and carboxylate ligands [15,16]. On the other hand, when magnetic interactions between metal centers are weak, $-\Delta S_m$ is a linear superposition of each ion, giving $-\Delta S_m{}^{max} = nR\ln(2S + 1)$ (n is the number of paramagnetic centers). In contrast, strong antiferromagnetic coupling reduces $-\Delta S_m$ due to the cancellation of adjacent magnetic moments, unless spin frustration [17] exists in the system; meanwhile, strong ferromagnetic coupling leads to a large ground-state spin that decreases entropy change to $R\ln(2nS + 1)$ [12,13]. The MCE performance of Gd^{3+}-based clusters depends on a delicate balance between magnetic ion density and exchange coupling. For example, **Gd$_{140}$** (M_W = 46730.00 g mol^{-1}, magnetic density N_{Gd}/M_W = 0.00300, Curie−Weiss constant $\theta = -2.4$ K) [15] shows $-\Delta S_m$ = 38.0 J kg^{-1} K^{-1} at 2 K for ΔH = 7 T, which is lower than **Gd$_{60}$**'s $-\Delta S_m$ of 48.0 J kg^{-1} K^{-1} ($\theta = -3.71$ K, N_{Gd}/M_W = 0.00302, M_W = 19871.97 g mol^{-1}) despite weaker antiferromagnetic coupling [16]. Conversely, **Gd$_{24}$** (M_W = 8169.48 g mol^{-1}, N_{Gd}/M_W = 0.00294, $\theta = -0.16$ K) [18], with the lowest magnetic ion density and weakest coupling, delivers $-\Delta S_m$ of 46.12 J kg^{-1} K^{-1} at 2.5 K and ΔH = 7 T, outperforming **Gd$_{140}$**.

Given the oxophilicity of lanthanide ions [19], employing oxygen-containing bidentate or multidentate ligands with controlled hydrolysis to generate $\mu_{2/3/4/5}$-O/OH groups promotes the aggregation of metal cores, which is one of the effective strategies for synthesizing structurally unique clusters [12,20,21]. However, synthesis involving heavier p-block elements, such as S atoms, is usually more challenging, primarily due to their reduced coordination affinity for lanthanide ions and the inherently less predictable/controllable nature of their coordination modes [22–26]. Notably, the larger atomic radii and diffuse p valence orbitals of these elements impart unique physicochemical properties to the resulting clusters [27,28], enabling structures ideal for studying magneto-structural relationships [29,30] and entropy change mechanisms. In complex cluster structures, when ligands containing heavy p-block elements coordinate in a terminal mode, they are likely to increase certain key parameters—such as intermetallic distances and metal–ligand bond lengths/angles—that directly influence magnetic coupling [31]. A substantial increase in the distance between Gd^{3+} ions, for example, may promote magnetic decoupling and reduce exchange pathways [32], ultimately leading to a significantly enhanced magnetic entropy change. Conversely, when ligands containing heavy p-block elements coordinate in a bridging mode, the diffuse p orbitals can facilitate stronger magnetic exchange coupling, thereby improving the relaxation dynamics in single-molecule magnets (SMMs) [33]. Additionally, strategic placement of soft S donors in the equatorial plane effectively weakens the transverse component of the crystal field, which contributes to enhanced SMM performance [27–30].

To this end, we employed 2-pyridinethiol 1-oxide (HL), a rarely explored ligand in lanthanide chemistry [34–40] that features both O and S donor sites, to construct lanthanide-based clusters. Using solvothermal methods, we successfully synthesized a new family of Ln_9 clusters $[Ln_9(L)_{17}(\mu_3\text{-OH})_9(\mu_4\text{-OH})]\cdot nH_2O$ (**1**: Ln = Gd, n = 3; **2**: Ln = Tb, n = 3; **3**: Ln = Dy, n = 1). Single-crystal X-ray diffraction analysis reveals that the nine metal centers adopt an hourglass geometric configuration in space. Magnetic studies of clusters **1**–**3** show distinct behaviors: cluster **1** features dominant antiferromagnetic interactions

and a significant MCE with $-\Delta S_m$ = 34.41 J kg^{-1} K^{-1} at ΔH = 7 T and 2 K, while cluster **3** exhibits SMM behavior. This family enables comparison with previously reported MCE of Ln_9 clusters supported by O/N donor ligands [41–43] and helps to understand the influence of S coordination on cluster assembly and magnetic properties.

2. Materials and Methods

2.1. Materials and Characterization

All the starting materials were commercially available reagents of analytical grade and were used without further purification. 2-pyridinethiol 1-oxide was purchased from Aladdin, Shanghai, China; $LnCl_3 \cdot 6H_2O$ (Ln = Gd, Tb, Dy) were purchased from 3A Material, Anqing, Anhui, China; triethylamine, and all solvents were purchased from Energy Chemical, Shanghai, China. Elemental analyses (C, N, H, and S) were carried out on a EUROVECTOR EA3000 elemental analyzer (Euro Vector, Sesena Comasco, MI, Italy). The powder X-ray diffraction (PXRD) measurements were recorded on a Bruker D8 ADVANCE X-ray diffractometer (Bruker, Karlsruhe, BW, Germany). Direct-current (dc) magnetic susceptibilities were measured on a Quantum Design MPMS-squid VSM magnetometer (Quantum Design, San Diego, CA, USA). Diamagnetic corrections were made with Pascal's constants for all the constituent atoms and the sample holder. Alternating-current (ac) magnetic susceptibility data were collected on the same instrument employing a 1.5 Oe oscillating field at frequencies up to 1000 Hz.

2.2. Syntheses of Complexes **1**–**3**

$[Gd_9(L)_{17}(\mu_3\text{-}OH)_9(\mu_4\text{-}OH)] \cdot 3H_2O$ (**1**): A mixture of $GdCl_3 \cdot 6H_2O$ (185.85 mg, 0.5 mmol), ligand HL (127.16 mg, 1.0 mmol; HL = 2-pyridinethiol 1-oxide), 278.0 µL of triethylamine (2.0 mmol), and 8 mL of CH_3OH was sealed in a Teflon-lined autoclave, which was heated at 130 °C for 24 h. After cooling to room temperature in 48 h, light-yellow block crystals of **1** suitable for single-crystal X-ray diffraction analysis were obtained. The crystals were washed with methanol (5 × 4.0 mL) and subsequently examined under an optical microscope to separate the white flocculent impurities from the target crystals. Drying the crystals under air at room temperature afforded a desolvated and hydrated species that was analyzed as **1**. Yield: 49.6% (based on Gd). Elemental analysis calcd (%) for **1** ($C_{85}H_{84}N_{17}S_{17}Gd_9O_{30}$): C 26.98, N 6.29, H 2.24, S 14.41; found: C 26.69, N 6.30, H 2.36, S 13.92.

$[Tb_9(L)_{17}(\mu_3\text{-}OH)_9(\mu_4\text{-}OH)] \cdot 3H_2O$ (**2**): This compound was synthesized by the same method as **1**, except that $GdCl_3 \cdot 6H_2O$ was replaced with $TbCl_3 \cdot 6H_2O$, affording light-yellow block crystals. The crystals were washed with methanol (5 × 4.0 mL) and subsequently examined under an optical microscope to separate the white flocculent impurities from the target crystals. Drying the crystals under air at room temperature afforded a desolvated and hydrated species that was analyzed as **2**. Yield: 38.7% (based on Tb). Elemental analysis calcd (%) for **2** ($C_{85}H_{84}N_{17}S_{17}Tb_9O_{30}$): C 26.87, N 6.27, H 2.23, S 14.35; found: C 26.73, N 6.26, H 2.20, S 13.92.

$[Dy_9(L)_{17}(\mu_3\text{-}OH)_9(\mu_4\text{-}OH)] \cdot H_2O$ (**3**): This compound was synthesized by the same method as **1**, except that $GdCl_3 \cdot 6H_2O$ was replaced with $DyCl_3 \cdot 6H_2O$, affording light-yellow block crystals. The crystals were washed with methanol (5 × 4.0 mL) and subsequently examined under an optical microscope to separate the white flocculent impurities from the target crystals. Drying the crystals under air at room temperature afforded a desolvated species that was analyzed as **3**. Yield: 42.8% (based on Dy). Elemental analysis calcd (%) for **3** ($C_{85}H_{80}N_{17}S_{17}Dy_9O_{28}$): C 26.90, N 6.27, H 2.12, S 14.36; found: C 26.54, N 6.76, H 2.24, S 14.22.

2.3. Single-Crystal Structure Determination

Single-crystal X-ray diffraction data were recorded on a Bruker D8 Venture diffractometer (Bruker, Karlsruhe, BW, Germany) with MoKα radiation. Diffraction data for crystals of **1**, **2**, and **3** were collected at 150 K using the APEX4 program. The structures were solved by the SHELXT-2024 software package and refined using a full-matrix least-squares method on F^2 with anisotropic thermal parameters for all nonhydrogen atoms. Hydrogen atoms were located geometrically and refined with a riding model with relative isotropic displacement parameters. Structural refinement revealed disorder and pronounced thermal motion in some lattice solvent molecules, triggering CheckCIF alerts (e.g., missing O–H acceptors). These effects are common in highly solvated crystals and do not compromise the integrity of the main framework. Details can be found in the Cambridge Crystallographic Data Centre using the CCDC numbers 2475935 (**1**), 2475936 (**2**), and 2475937 (**3**).

3. Results and Discussion

3.1. Crystal Structure

Single-crystal X-ray diffraction analyses reveal that complexes **1** and **2** are isostructural, both crystallizing in the triclinic *P*-1 space group, whereas complex **3** crystallizes in the monoclinic $P2_1/c$ space group (Table S1). Thus, the structures of complexes **1** and **3** are described in detail.

The asymmetric units of both complexes **1** and **3** feature nine metal ions, seventeen L^- ligands, nine μ_3-OH and one μ_4-OH groups, and some free solvent molecules. The eight Ln^{3+} (Ln1–Ln4 and Ln6–Ln9, Ln = Gd, Dy) ions occupy the vertices of a square antiprism, and the ninth (Ln5) resides at its geometric center, forming a canonical hourglass geometric configuration. This configuration consists of two quadrilateral base planes and eight triangular planes, resulting in an $[Ln_9(\mu_3\text{-OH})_9(\mu_4\text{-OH})]^{17+}$ core encapsulated by seventeen bidentate L^- ligands. To facilitate the description of ligand coordination modes, three types are identified: (1) μ_1-η^1:η^1: terminal bidentate coordination through both S and O donors to a single lanthanide center; (2) μ_2-η^1:η^2: monodentate S-coordination to one lanthanide ion coupled with μ_2-O bridging to a neighboring metal center; and (3) μ_2-η^1:η^2: monodentate O-coordination to one lanthanide ion accompanied by μ_2-S bridging to an adjacent metal ion (Figure 1).

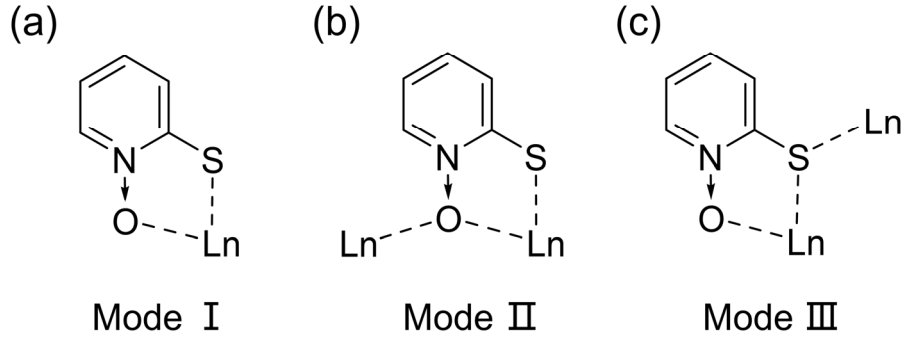


Figure 1. Ligand coordination modes: Modes I (**a**), II (**b**), and III (**c**).

In complex **1**, a μ_4-OH group bridges the four Gd^{3+} ions (Gd1–Gd4) of the upper quadrilateral base plane (O atom 0.57 Å above the plane (Figure 2a); adjacent Gd···Gd distances in the range of 3.6107(6)–3.6700(6) Å). Adjacent Gd^{3+} ions in this plane are further interconnected by μ_2-η^1:η^2 bridges from ligand L^- (Mode II: μ_2-O and monodentate S), with the exception of the Gd1–Gd4 edge, where ligand disorder results in mixed μ_2-η^1:η^2 bridging (approximately 60% Mode II (μ_2-O) and 40% Mode III (μ_2-S)) (Figure 3a). Four μ_3-OH groups connect the upper quadrilateral plane to Gd5, forming four triangular planes.

The Gd1–Gd4 ions are all eight-coordinate (Figure S1), adopting a triangular dodecahedron (D_{2d}) local geometric configuration as determined by the SHAPE 2.1 software [44] (Table S2), with each coordination sphere containing two μ_2-η^1:η^2 ligands, one μ_1-η^1:η^1 ligand, one μ_4-OH, and two μ_3-OH groups. The central Gd5 ion occupies the geometric center, coordinated to eight μ_3-OH groups that connect it to both the upper (Gd1–Gd4) and lower (Gd6–Gd9) quadrilateral planes, adopting a square antiprism (D_{4d}) local geometry. The centers of the two quadrilateral base planes are separated by 5.5476 (2) Å with an interplanar torsion angle of 47.318(105)°. The lower quadrilateral base plane (Gd6–Gd9) exhibits distinct structural features (Figure S1). A μ_3-OH group (O atom 0.53 Å below the plane) bridges Gd6, Gd7, and Gd9, while the plane displays significant distortion from ideal square geometry (adjacent Gd···Gd distances ranging from 3.5658(7) to 3.9598(7) Å and the bond lengths of Gd–μ_3-O varying between 2.413(4) and 2.540(1) Å; Tables S3 and S4). This geometric asymmetry results in varied coordination environments for Gd6–Gd9 compared to the more symmetric upper Gd1–Gd4 plane, highlighting the overall molecular asymmetry. While adjacent Gd^{3+} ions in the lower plane are similarly interconnected by μ_2-η^1:η^2 bridges from ligand L^- (Mode II: μ_2-O and monodentate S), their coordination environments diverge significantly. Gd6 and Gd7 maintain eight-coordinate triangular dodecahedron (D_{2d}) geometries, each binding to two μ_2-η^1:η^2 ligands (combing one S atom and two μ_2-O), one μ_1-η^1:η^1 L^- ligand, and three μ_3-OH groups. In contrast, Gd9 expands to nine-coordination through two μ_2-η^1:η^2 modes (two S atoms and two μ_2-O), one μ_1-η^1:η^1 L^- ligand, and three μ_3-OH groups, resulting in a spherical capped square antiprism (C_{4v}) local geometry. Gd8 remains eight-coordinate with a triangular dodecahedron (D_{2d}) local geometry but exhibits a distinct arrangement, coordinating to two μ_2-O donors (from two μ_2-η^1:η^2 L^-), two μ_1-η^1:η^1 L^- ligands, and two μ_3-OH groups.

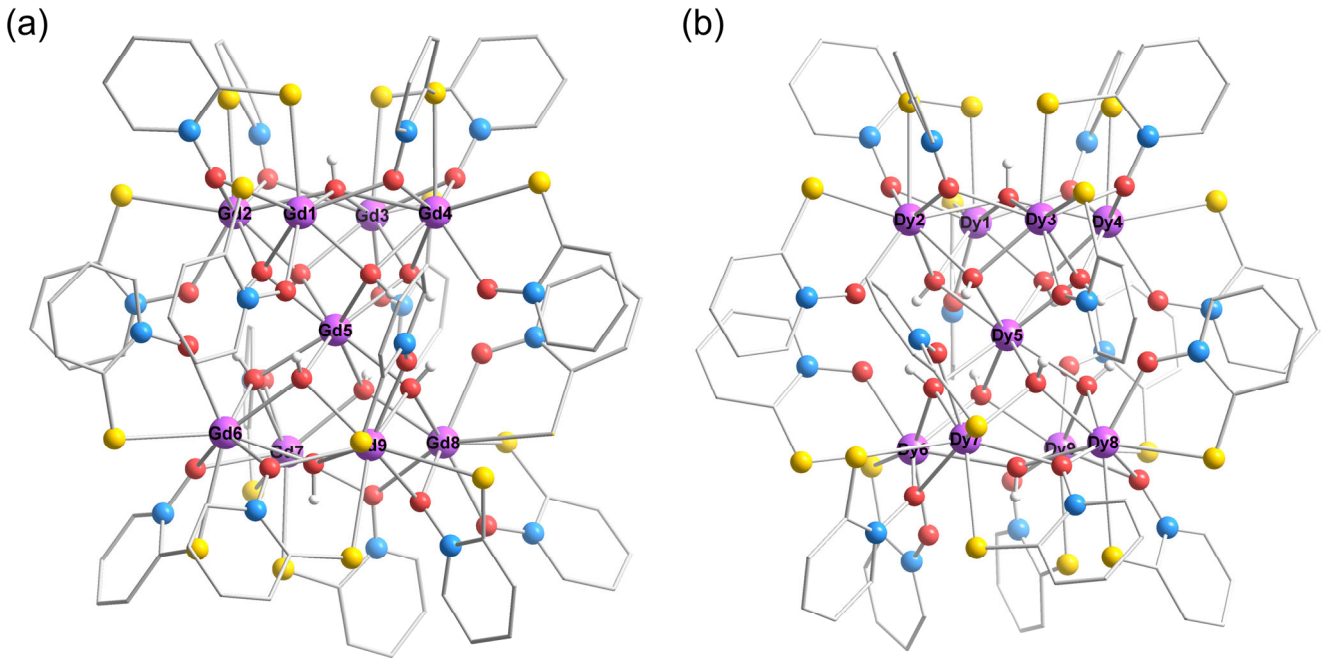


Figure 2. The crystal structure diagram of **1** (**a**) and **3** (**b**). Color code: O (red), C (gray), N (blue), Gd/Dy (purple), S (yellow), and H (white). A disordered L^- with μ_2-S (Mode III) coordination in **1,** disordered L^- ligands in **3**, and free solvent molecules and hydrogen atoms of pyridine rings in **1** and **3** are omitted for clarity.

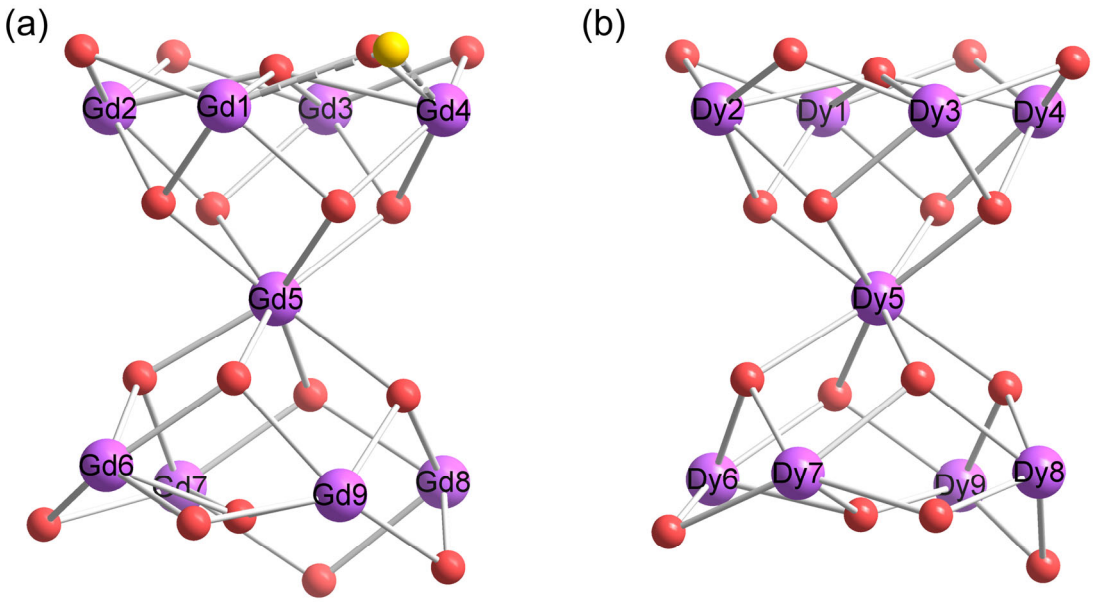


Figure 3. Representation of the core structure of **1** (**a**) and **3** (**b**). Color code: O (red), Gd/Dy (purple), and S (yellow). The gray dotted line represents the disordered components within the structure.

According to the packing diagram (Figure S2), the shortest intermolecular Gd···Gd distance is 9.0353(7) Å. The presence of hydroxyl groups and solvent molecules within the cluster forms intra- and intermolecular hydrogen bonds (Table S5). Further analysis reveals that the pyridine rings mediate intra- and intermolecular π···π stacking (dihedral angle < 20°) (Table S6) and intermolecular C–H···π interactions, with distances between the hydrogen atoms and the ring centroids ranging from 2.68 to 2.98 Å (Table S7). These noncovalent interactions notably enhance the thermal and structural stability of the air-stable metal clusters.

In complex **3**, the spatial arrangement of metal ions (Dy1–Dy9) and their linkage pattern across the eight triangular planes are identical to those in complex **1**, forming a $[Dy_9(\mu_3\text{-OH})_9(\mu_4\text{-OH})]^{17+}$ core structure (Figures 2b and 3b). Notably, all Dy^{3+} ions are eight-coordinate. Dy1−Dy5 display coordination geometries that closely resemble those of their Gd^{3+} analogs (Gd1–Gd5), with Dy1–Dy4 adopting D_{2d} local geometries and Dy5 exhibiting a D_{4d} geometry (Table S8). Dy9 shows identical coordination to Gd6 and Gd7 (Figure S3), also featuring a D_{2d} local geometry. However, Dy6 and Dy7 share a distinct coordination sphere comprising one μ_3-OH from the lower plane, two μ_3-OH bridges to central Dy5, one μ_2-O donor (from one μ_2-η^1:η^2 L^-), and two μ_1-η^1:η^1 L^- ligands (Figure S4). Despite this similarity, their local geometries differ slightly, adopting D_{4d} and D_{2d} configurations, respectively. Dy8 adopts a unique environment, coordinated by two μ_3-OH groups, two μ_2-η^1:η^2 L^- ligands (containing two S and two μ_2-O), and one μ_1-η^1:η^1 L^- ligand, exhibiting a D_{2d} local geometry. The adjacent Dy···Dy distances for Dy6–Dy9 range from 3.5824(7) to 3.8408(7) Å, and the Dy−μ_3-O bond lengths display a wider variation (2.470(5)–2.715(5) Å) than those found in **1** (Tables S9 and S10). The packing analysis reveals that the shortest intermolecular Dy···Dy distance is 9.8618(6) Å (Figure S5), longer than that in **1**. The structure also features an enhanced hydrogen bonding network (Table S5). Notably, the pyridine rings are only engaged in intramolecular π···π stacking (Table S6) and intermolecular C–H···π interactions, with distances between the hydrogen atom and the ring centroid ranging from 2.66 to 2.85 Å (Table S7).

Overall, in contrast to previously reported symmetric hourglass-like Ln_9 clusters [24,41–43,45–69], the present Ln_9 family exhibits significant structural asymmetry: Ln1–Ln4 and Ln6–Ln9 differ entirely in coordination environments, while the upper and

lower basal planes feature different bridging modes (μ_4-OH and μ_3-OH, respectively). To facilitate subsequent studies on magneto-structural relationships, we compared cluster **1** with four previously reported Gd_9 clusters that exhibit MCE [41–43]. Gd1–Gd5 share similar bridging modes: adjacent Gd1–Gd4 ions are connected by μ_2-O bridges (Gd···Gd distance ≈ 3.6 Å) with a central μ_4-OH group (diagonal Gd···Gd distance in the upper plane ≈ 5.2 Å), while Gd5 links to eight Gd^{3+} ions via eight μ_3-OH bridges ($Gd_{1–4}$···Gd_5 distance ≈ 3.8 Å). Despite these similarities in connectivity and distances, cluster **1** exhibits distinct bond angles compared to the four cases: its adjacent Gd–μ_2-O–Gd angles for Gd1–Gd4 (96.1–100.6°) are in a medium range (Table S11), its diagonal Gd–μ_4-O–Gd angles in the upper plane (155.2–156.2°) are smaller, and its $Gd_{1–4}$–μ_3-O–Gd_5 angles (107.0–108.1°) show a larger average (Table S11). These differences become even more pronounced in Gd6–Gd9, which display greater variation in adjacent Gd···Gd distances (3.6–4.0 Å) with Gd–μ_2-O–Gd angles (93.3–107.1°, Table S11). Here, the diagonal Gd6···Gd8 and Gd7···Gd9 distances are 5.7 Å and 4.8 Å, respectively, and the $Gd_{6–9}$–O–Gd_5 angles range from 102.4 to 109.9°. Considering that the key difference in cluster **1** lies in the partial replacement of conventional N/O donors by S atoms from the ligands, with a disordered segment containing μ_2-S bridging Gd1 and Gd4, we propose that the asymmetric structure and variations in bond angles and Gd···Gd distances likely arise from the coordination and bridging of sulfur-containing ligands.

The powder X-ray diffraction patterns of polycrystalline samples of **1** and **2** are distinctly different from that of **3**, matching well with their respective single-crystal X-ray diffraction simulations (Figure S6). This agreement confirms the high phase purity of all samples.

3.2. Magnetic Properties

Variable-temperature magnetic susceptibility measurements of complexes **1–3** were performed on polycrystalline samples under a 1 kOe direct current (dc) magnetic field over the temperature range of 2–300 K. At 300 K, the $\chi_M T$ products for complexes **1–3** are 68.26, 104.02, and 125.64 cm^3 K mol^{-1}, respectively (Figure 4a), in close agreement with the theoretical values calculated for non-interacting magnetic centers: 70.92 $cm^3 \cdot K \cdot mol^{-1}$ for nine independent Gd^{3+} ions ($S = 7/2$, $g = 2.0$), 106.38 $cm^3 \cdot K \cdot mol^{-1}$ for nine isolated Tb^{3+} ions ($S = 3$, $g = 3/2$), and 127.53 cm^3 K mol^{-1} for nine non-coupled Dy^{3+} ions ($S = 5/2$, $g = 4/3$). Upon cooling, complex **1** exhibits nearly constant $\chi_M T$ values above 80 K, reflecting the dominant paramagnetic behavior of non-interacting Gd^{3+} ions; below 80 K, $\chi_M T$ decreases gradually before undergoing a steep decline to 34.66 cm^3 K mol^{-1} at 2 K, indicating the onset of antiferromagnetic interactions. Curie–Weiss analysis (2–300 K) yields Curie constant C = 69.35 cm^3 K mol^{-1} and Curie temperature $\theta = -2.15$ K, with the negative θ confirming antiferromagnetic interactions between metal ions (Figure 4b). Complex **2** exhibits a subtle decrease in $\chi_M T$ above 100 K, while complex **3** shows a more pronounced reduction in this regime. Both systems undergo progressive declines followed by steep reductions below 50 K, reaching minima of 39.12 and 76.30 cm^3 K mol^{-1} at 2 K for **2** and **3**, respectively. This behavior originates from thermal depopulation of Stark sublevels, with potential contributions from weak antiferromagnetic exchange.

To further explore the magnetic interactions between Gd^{3+} ions in **1**, we classify the exchange pathways into six distinct types (J_1–J_6) based on their bridging motifs (Figure 5a). The magnetic interaction denoted as J_1 stems from the coupling between Gd1 and Gd2, which are bridged by one μ_4-OH, one μ_3-OH, and a μ_2-O ligand. Notably, ligand disorder along the Gd1–Gd4 edge, which leads to a mixed μ_2-η^1:η^2 bridging mode, is not specifically considered in the magnetic model, similar to J_1. J_2 characterizes the diagonal magnetic interaction between Gd^{3+} ions in the upper Gd1–Gd4 quadrilateral base plane

via a μ_4-OH bridge. J_3 describes the magnetic interaction between Gd5 and its adjacent Gd^{3+} ions through two μ_3-OH groups. J_4 accounts for the magnetic coupling between Gd^{3+} ions mediated by two μ_3-OH and one μ_2-O ligand. J_5 quantifies the interaction between adjacent Gd^{3+} ions bridged by one μ_3-OH and one μ_2-O ligand. Finally, J_6 defines the magnetic exchange interaction between Gd7 and Gd9, which are connected by a single μ_3-OH bridge. Thus, the spin Hamiltonian of the system is derived by integrating these exchange interactions.

$$\hat{H} = -2J_1(S_1S_2 + S_2S_3 + S_3S_4 + S_1S_4) - 2J_2(S_1S_3 + S_2S_4) - 2J_3(S_1S_5 + S_2S_5 + S_3S_5 + S_4S_5 + S_6S_5 + S_7S_5 + S_8S_5 + S_9S_5) - 2J_4(S_6S_7 + S_6S_9) - 2J_5(S_7S_8 + S_9S_8) - 2J_6(S_7S_9) \quad (1)$$

In this model, S_1–S_9 represent the spin of Gd1–Gd9, respectively, where positive values of J indicate ferromagnetic interactions, and negative values correspond to antiferromagnetic interactions.

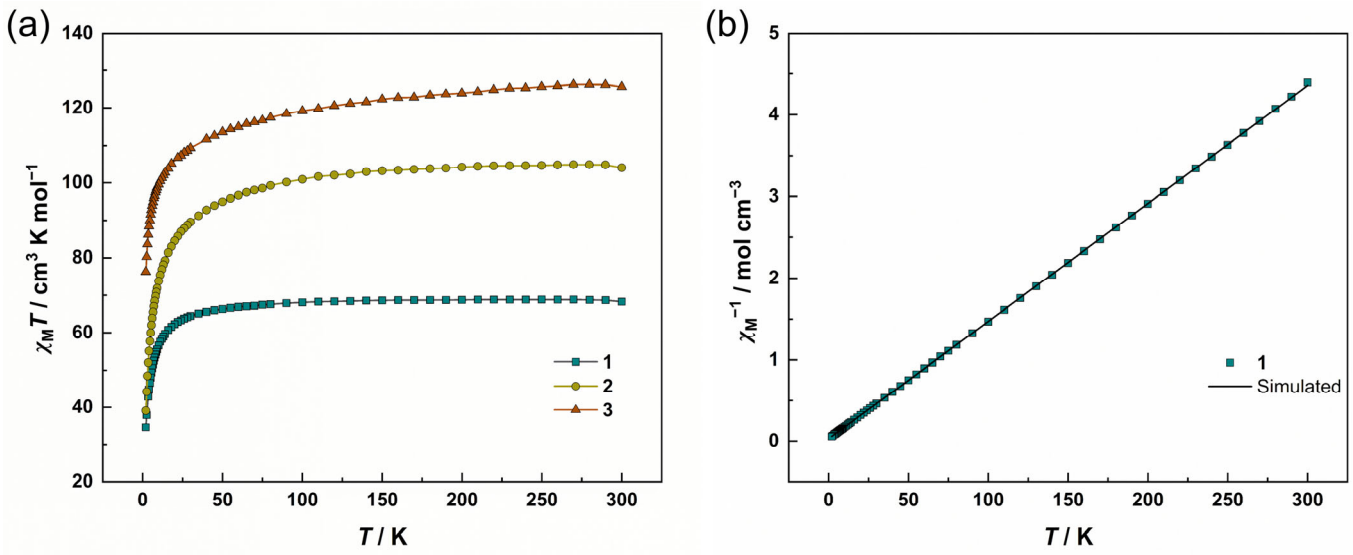


Figure 4. (**a**) Temperature-dependent susceptibilities for **1**–**3** under a dc magnetic field of 1000 Oe; (**b**) the $\chi_M{}^{-1}$ vs. T plot of **1**. The solid black line represents the best fits with the Curie–Weiss law.

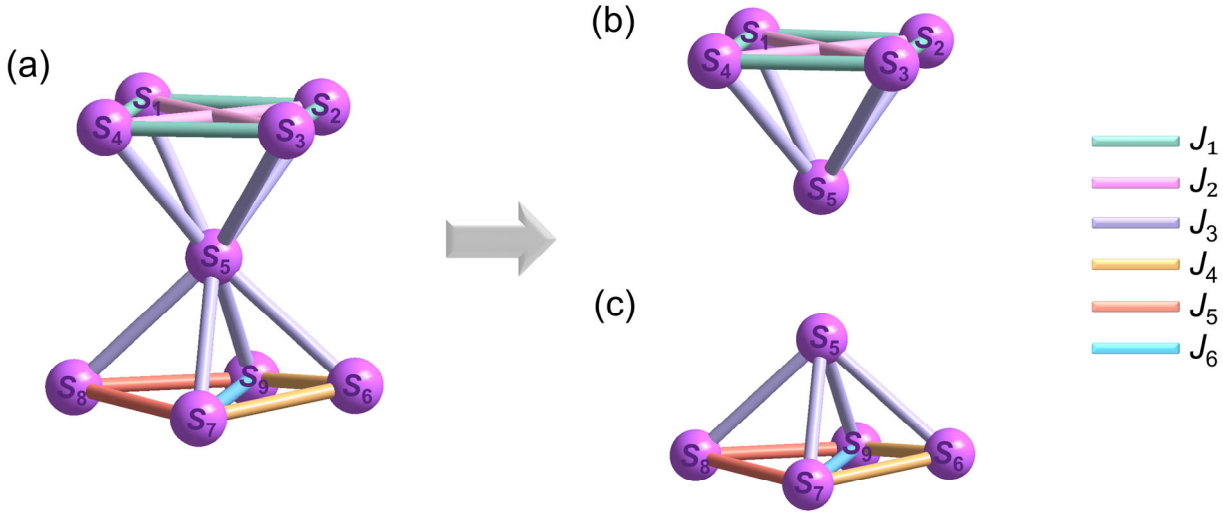


Figure 5. Magnetic coupling schematic diagram of **1** (**a**), **Gd_5** including Gd1–Gd5 (**b**), and **Gd_5** including Gd5–Gd9 (**c**) systems in **1**. Color code: Gd (purple), J_1 (cyan), J_2 (pink), J_3 (light purple), J_4 (yellow), J_5 (orange), and J_6 (blue).

To address computational challenges in modeling the magnetic properties of a nonanuclear cluster, we implement a reduced pentanuclear approximation. Given the prohibitively large exchange matrix for the full Gd_9 system, we strategically retain the core magnetic unit comprising the central Gd5 ion and four vertex ions (Gd_5: Gd1–Gd4 from the upper plane or Gd6–Gd9 from the lower plane) (Figure 5b,c). This simplification exploits the inherent S_4 symmetry of the cluster, where Gd5 occupies the inversion center and the upper/lower Gd_4 planes exhibit congruent coordination environments. The resultant Hamiltonian matrix enables computationally tractable fitting while preserving the dominant exchange pathways.

$$\hat{H} = -2J_1(S_1S_2 + S_2S_3 + S_3S_4 + S_1S_4) - 2J_2(S_1S_3 + S_2S_4) - 2J_3(S_1S_5 + S_2S_5 + S_3S_5 + S_4S_5) \quad (2)$$

$$\hat{H} = -2J_3(S_6S_5 + S_7S_5 + S_8S_5 + S_9S_5) - 2J_4(S_6S_7 + S_6S_9) - 2J_5(S_7S_8 + S_9S_8) - 2J_6(S_7S_9) \quad (3)$$

Considering the approximate treatments applied during the fitting, the $\chi_M T$ data for both Gd_5 models were derived by converting the $\chi_M T$ values of **1** (M_W = 3784.03 g mol^{-1}): $\chi_M T$ (Gd_5) = $\chi_M T$ (**1**)/9 × 5 (Figure S7). The optimal fitting of the experimental $\chi_M T$ vs. T data yields the magnetic parameters $J_1 = -0.055$ cm^{-1}, $J_2 = -0.114$ cm^{-1}, $J_3 = 0.019$ cm^{-1}, and $g = 1.979$ using Equation (2), and $J_3 = 0.015$ cm^{-1}, $J_4 = -0.097$ cm^{-1}, $J_5 = -0.082$ cm^{-1}, $J_6 = -0.072$ cm^{-1}, and $g = 1.980$ using Equation (3) [70]. These results are consistent with established magneto-structural relationships [42,71,72]. The ferromagnetic J_3 coupling originates from μ_3-OH bridges, aligning with empirical models where the Gd–O–Gd bond angles between 105 and 135° favor ferromagnetic interactions in Gd1–Gd5 (Table S4, bold font) [42,71,72]. However, in Gd5–Gd9, only 62.5% of the Gd–O–Gd bond angles fall within the 105–135° range. This may account for the smaller magnitude of the J_3 in Equation (3) compared to that in Equation (2). In contrast, the antiferromagnetic J_1, J_2, J_4, and J_6 arise from μ_4-OH/μ_3-OH/μ_2-O bridges, which is consistent with the correlation that excessively large or small bond angles result in antiferromagnetic coupling (Table S4, underlined font and wavy font, respectively). Compared with other hourglass-like Ln_9 clusters [24,41–43,45–69], the structural differences in compound **1**—beyond variations in ligands and symmetry—are mostly reflected in bond angles and Gd···Gd distances. For the upper base, the presence of μ_4-OH bridging groups restricts the ability of sulfur-containing ligands to modify the distances between central metal ions during coordination. For the lower base, however, as only three Gd^{3+} ions are connected by one μ_3-OH bridging group, the influence of sulfur-containing ligands becomes more prominent. They widen the Gd···Gd distances (Gd7···Gd8 = 3.96 Å, Gd8···Gd9 = 3.87 Å), make contributions to reducing magnetic exchange pathways [32], and also affect the distribution of Gd–O–Gd bond angles (Table S11). All these factors directly influence the magnetic coupling between metal ions.

The field-dependent magnetization of complex **1** was measured at discrete temperatures (2–10 K) under applied magnetic fields up to 7 T (Figure 6a). The magnetization (M) versus field curves exhibit a nearly linear increase at low fields (< 2 T), followed by a gradual approach to saturation, reaching a value of 62.13 Nβ at 2 K and 7 T, which is in close agreement with the theoretical saturation magnetization of 63 Nβ for nine non-interacting Gd^{3+} ions. Given the weak magnetic interactions observed in **1** and the well-known MCE in Gd^{3+}-based clusters, the $-\Delta S_m$ values were calculated by the magnetic data using the Maxwell equation:

$$\Delta Sm(T) = \int [\partial M(T, H)/\partial T]_H dH \quad (4)$$

where T is the testing temperature, H is the applied magnetic field, and M is magnetization.

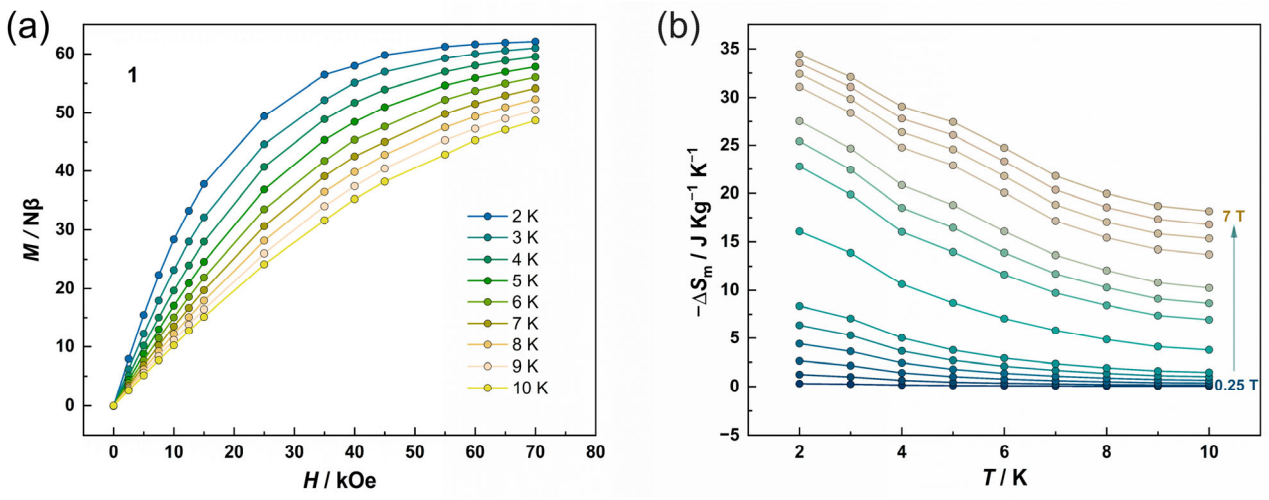


Figure 6. (**a**) Plots of M vs. H at various temperatures for **1**. (**b**) Plots of experimental magnetic entropy change versus T for **1** at 0.25–7 T from 2 to 10 K.

As shown in Figure 6b, the $-\Delta S_m$ values demonstrate a monotonic increase with decreasing temperature and increasing magnetic field change (ΔH), reaching a maximum value of $-\Delta S_m$ = 34.41 J kg^{-1} K^{-1} at 2 K under ΔH = 7 T (Figure 6b). This value is approximately 84% of the theoretical limit of 41.2 J kg^{-1} K^{-1} calculated by $-\Delta S_m{}^{max} = nR\ln(2S + 1)/M_W$, with the reduction primarily attributed to the presence of weak interactions between adjacent metal ions. Notably, while moderate among molecular magnetic coolers generally [4,8–11], this $-\Delta S_m$ value ranks as the second highest reported for Gd_9 clusters (Table S12). When the number of central metal ions is the same, magnetic density—a key parameter that determines entropy change—can be readily inferred from the molecular weight. For instance, **1** has the largest molar mass (M_W = 3784.03 g mol^{-1}), corresponding to the lowest value of N_{Gd}/M_W among these Gd_9 clusters [41,42]. In MCE materials research, a larger molar mass and lower magnetic density are generally considered unfavorable for achieving high $-\Delta S_m$ values, as a lower concentration of magnetic ions per unit mass tends to limit the degree of magnetic ordering that contributes to entropy change under an external magnetic field [4]. Despite this, **1** exhibits a $-\Delta S_m$ value comparable to that of $Gd_9(L^1)_4(\mu_4\text{-OH})_2(\mu_3\text{-OH})_8(\mu_2\text{-OCH}_3)_4(NO_3)_8(H_2O)_8\}(OH)\cdot 2H_2O$ (HL^1 = 2,6-dimethoxyphenol, M_W = 3015.28 g mol^{-1}). This compound, although not the lightest, displays weak antiferromagnetic and ferromagnetic interactions and holds the highest $-\Delta S_m$ value (40.60 J kg^{-1} K^{-1} at 2 K under ΔH = 7 T) reported for Gd_9 clusters to date (Table S12) [41–43]. Meanwhile, **1** has a $-\Delta S_m$ slightly larger than that of the third-ranked cluster, $[Gd_9(L^2)_4(NO_3)_{12}(\mu_3\text{-OH})_8(\mu_4\text{-OH})_2(CH_3CH_2OH)_4]\cdot 4.5CH_3CH_2OH\cdot 3Et_3NH$ (H_2L^2 = *N*-methyldiethanolamine, M_W = 3288.90 g mol^{-1}, $-\Delta S_m$ = 33.65 J kg^{-1} K^{-1} at 3 K under ΔH = 7 T) [41], and much larger than that of the fourth-ranked cluster, $[Gd_9(L^3)_8(NO_3)_8(\mu_3\text{-OH})_8(\mu_4\text{-OH})_2]\cdot NO_3$ (HL^3 = 2-(2-aminoethoxy)ethanol; acac = acetylacetonate; M_W = 2976.45 g mol^{-1}, $-\Delta S_m$ = 25.22 J kg^{-1} K^{-1} at 3 K under ΔH = 7 T) [41] with the highest magnetic density and lowest molecular weight in Gd_9 clusters with MCE (Table S12).

Research findings reveal that both magnetic density and magnetic interactions affect the $-\Delta S_m$ value. For complex **1**, magnetic density seems to play a minor role in determining the large $-\Delta S_m$. We thus propose three potential factors contributing to its enhanced magnetocaloric performance. First, the incorporation of the heavy p-block S atoms from the HL ligands alters the cluster architecture, particularly affecting the Gd^{3+} ions at the vertices of the upper and lower basal planes, which are bridged by a μ_4-OH and μ_3-OH, respectively. Next, these sulfur-containing ligands in terminal coordination mode modu-

late key structural parameters—specifically Gd–$\mu_2/\mu_3/\mu_4$-O–Gd bond angles and Gd···Gd distances—rendering the structure distinct from previously reported Gd_9 clusters ligated solely by N/O donors. Last, these geometric perturbations are expected to influence the nature and strength of magnetic exchange pathways, including both ferromagnetic and antiferromagnetic interactions. Collectively, these effects enhance the magnetic entropy change, despite the higher atomic mass of sulfur compared to conventional N/O-coordinating atoms.

Magnetization versus field measurements for complex **2** at 2 K reveal a gradual increase to a maximum moment of 46.31 Nβ at 7 T without a saturation plateau (Figure S8). Alternating-current (ac) magnetic susceptibility measurements under zero dc field with an oscillating field of 1.5 Oe show no detectable out-of-phase magnetic susceptibility (χ'') signal down to 2 K, suggesting the absence of magnetic relaxation (Figure S9). Consistently, hysteresis measurements at 2 K at a sweep rate of 200 Oe s^{-1} exhibit vanishingly small coercivity (Figure S10). This collective behavior precludes SMM behavior under these conditions.

Magnetization versus field measurements for complex **3** at 2 K show a gradual approach to 50.91 Nβ at 7 T (Figure S11). The absence of distinct saturation and temperature-dependent non-superposition of $M(H)$ curves possibly originates from strong intrinsic magnetic anisotropy. Frequency dependence of χ'' under 12 K confirms the slow magnetic relaxation characteristic of SMM behavior (Figures 7 and S12). However, the absence of a discernible peak in the χ'' signal prevents the determination of relaxation time and thus the relaxation energy barrier. This behavior is similar to most reported nonanuclear Dy^{3+}-based compounds [48,50,56,63]—except for one Dy_9 compound with an energy barrier of U_{eff} = 9.24 K [47]. Zero-field-cooled and field-cooled (ZFC–FC) susceptibility measurements at H = 50 Oe show no divergence, ruling out long-range magnetic ordering or superparamagnetic transitions (Figure S13). Additionally, hysteresis measurements at 2 K at a sweep rate of 200 Oe s^{-1} exhibit minimal coercivity (Figure S14).

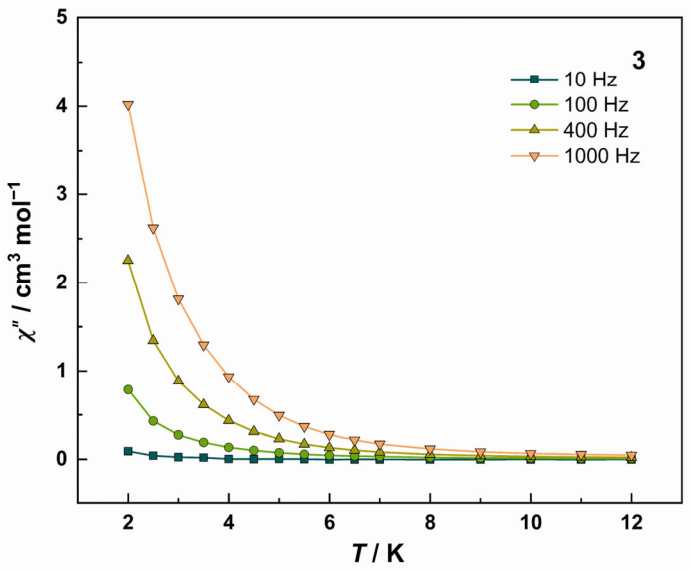


Figure 7. Temperature dependence of the χ'' ac susceptibility for **3** under zero dc field in the temperature range of 2–12 K.

4. Conclusions

In summary, three nonanuclear lanthanide-based clusters $[Ln_9(L)_{17}(\mu_3\text{-}OH)_9(\mu_4\text{-}OH)]\cdot nH_2O$ (**1**: Ln = Gd, n = 3; **2**: Ln = Tb, n = 3; **3**: Ln = Dy, n = 1) were synthesized under hydrothermal conditions with sulfur-containing bidentate ligand 2-pyridinethiol 1-oxide. Remarkably, all three clusters exhibit a unique asymmetric architecture in which the upper and lower Ln_9 cores are bridged by μ_4-OH and μ_3-OH groups, respectively. Of these three

clusters, **1** exhibits an excellent cryogenic MCE with $-\Delta S_m$ = 34.41 J kg^{-1} K^{-1} at 2 K under ΔH = 7 T, and **3** shows the SMM behavior. It is worth noting that, compared with the other four reported Gd_9 clusters with MCE, **1** exhibits a magnetic entropy change value that is second only to the highest among Gd_9 systems, despite having the largest molar mass and the lowest magnetic density, indicating the dominant role of magnetic coupling in determining the magnetocaloric performance. Specifically, the sulfur-containing bidentate ligands, coordinated in a terminal mode, influence key structural parameters of the nonanuclear cluster, including increasing the distances between Gd^{3+} ions, modifying the Gd–O–Gd bond angles, and reducing the number of bridging groups. This work not only expands research on the MCE of Gd_9 clusters but also provides a new synthetic strategy for constructing high-performance molecular-based magnetic cooling materials using ligands containing heavy p-block elements.

Supplementary Materials: The following supporting information can be downloaded at https://www.mdpi.com/article/10.3390/magnetochemistry11090070/s1. Figure S1: The coordination environment diagram of compound **1**. Color code: O (red), Gd (purple), S (yellow), and H (white). A disordered L^- with μ_2-S (Mode III) coordination, free solvent molecules, and pyridine rings are omitted for clarity; Figure S2: The stacking pattern within a unit cell of **1**. Color code: O (red), C (gray), N (blue), Gd (purple), and S (yellow). Disordered L^- with μ_2-S, free solvent molecules, and H atoms are omitted for clarity; Figure S3: The part crystal structure diagram of compound **1** (**a**) and **3** (**b**) containing Ln6–Ln9. Color code: O (red), C (gray), N (blue), Gd/Dy (purple), S (yellow), and H (white). The extra carbon atoms on the pyridine rings with their hydrogen atoms and free solvent molecules are omitted for clarity; Figure S4: The coordination environment diagram of compound **3**. Color code: O (red), C (gray), N (blue), Dy (purple), S (yellow), and H (white). Disordered L^- ligands, free solvent molecules, and pyridine rings are omitted for clarity; Figure S5: The stacking pattern within a unit cell of **3**. Color code: O (red), C (gray), N (blue), Dy (purple), and S (yellow). Unordered L^- ligands, free solvent molecules, and H atoms are omitted for clarity; Figure S6: The PXRD curves of fresh samples of **1**–**3**. The two calculated curves are simulated from the single crystal data of **1** and **3**; Figure S7. Temperature dependence of χ_M and $\chi_M T$ for Gd_5: Gd1–Gd5 (**a**) and Gd5–Gd9 (**b**). The experimental data of Gd_5 were obtained by converting the data of **1**, while the solid lines represent the best fits through the PHI program [70]; Figure S8: The plot of M vs. H at 2 K for **2**; Figure S9: Temperature dependence of the in-phase (χ') (**a**) and out-of-phase (χ'') (**b**) ac susceptibility for **2** under zero dc field in the temperature range of 2–12 K; Figure S10: Hysteresis loop for **2** measured at 2 K with a sweep rate of 200 Oe/s; Figure S11: The plots of M vs. H at various temperatures for **3**; Figure S12: Temperature dependence of the in-phase (χ') (**a**) and out-of-phase (χ'') (**b**) ac susceptibility for **3** under zero dc field in the temperature range of 2–12 K; Figure S13: FC and ZFC of **3** at an applied field of 50 Oe; Figure S14: Hysteresis loop for **3** measured at 2 K with a sweep rate of 200 Oe/s. Illustration: an enlarged view of the area near the zero field. Table S1: Crystallographic data and structure refinement for **1**–**3**; Table S2: Continuous Shape Measures (CShMs) calculation for **1**; Table S3: Selected bond lengths (Å) for **1**; Table S4: Selected angles (deg) for **1**; Table S5: Hydrogen bonding parameters in clusters **1**–**3**; Table S6: π···π interaction parameters (Å, deg) for **1** and **3**; Table S7: C–H···π interaction parameters (Å, deg) for clusters **1** and **3**; Table S8: Continuous Shape Measures (CShMs) calculation for **3**; Table S9: Selected bond lengths (Å) for **3**; Table S10: Selected angles (deg) for **3**; Table S11: The selected Gd–O–Gd angles of the reported Gd9 clusters with MCE [41–43]; Table S12: The MCE properties of the previously reported Gd_9 clusters [41–43].

Author Contributions: Conceptualization, T.H.; methodology, Y.-W.G. and T.G.; investigation, Y.-W.G. and X.-Q.W.; data curation, T.G. and Y.-W.G.; writing—original draft preparation, Y.-W.G.; writing—review and editing, T.H.; supervision, T.H.; funding acquisition, T.H. Of the authors, Y.-W.G. and T.G. contributed equally to this work. All authors have read and agreed to the published version of the manuscript.

Funding: This research was funded by the National Natural Science Foundation of China (funding number: 22271228) and the Fundamental Research Funds for the Central Universities (funding number: xzy012023031).

Institutional Review Board Statement: Not applicable.

Informed Consent Statement: Not applicable.

Data Availability Statement: The original contributions presented in this study are included in the article and the Supplementary Materials.

Acknowledgments: We thank Chang Huang and Dan He at the Instrument Analysis Center of Xi'an Jiaotong University for assistance with single-crystal X-ray diffraction measurement and magnetic measurement, respectively.

Conflicts of Interest: The authors declare no conflicts of interest.

References

1. Lucia, U.; Grisolia, G. Magnetocaloric refrigeration in the context of sustainability: A review of thermodynamic bases, the state of the art, and future prospects. *Energies* **2024**, *17*, 3585. [CrossRef]
2. Zhao, S.; Wang, P.; Chen, W.; Wang, L.; Wang, Q.C.; Chen, W.Q. Supply and demand conflicts of critical heavy rare earth element: Lessons from gadolinium. *Resour. Conserv. Recycl.* **2023**, *199*, 1–9. [CrossRef]
3. Nehan, P.Z.Z.; Vitayaya, O.; Munazat, D.R.; Manawan, M.T.E.; Darminto, D.; Kurniawan, B. The magnetocaloric effect properties for potential applications of magnetic refrigerator technology: A review. *Phys. Chem. Chem. Phys.* **2024**, *26*, 14476–14504. [CrossRef]
4. Zheng, Y.-Z.; Zhou, G.-J.; Zheng, Z.; Winpenny, R.E.P. Molecule-based magnetic coolers. *Chem. Soc. Rev.* **2014**, *43*, 1462–1475. [CrossRef] [PubMed]
5. Pecharsky, V.K.; Gschneidner, K.A. Magnetocaloric effect and magnetic refrigeration. *J. Magn. Magn. Mater.* **1999**, *200*, 44–56. [CrossRef]
6. De Haas, W.J. Extremely low temperatures. *Nature* **1933**, *132*, 372–373. [CrossRef]
7. Phan, M.H.; Yu, S.C. Review of the magnetocaloric effect in manganite materials. *J. Magn. Magn. Mater.* **2007**, *308*, 325–340. [CrossRef]
8. Hu, J.J.; Peng, Y.; Liu, S.J.; Wen, H.R. Recent advances in lanthanide coordination polymers and clusters with magnetocaloric effect or single-molecule magnet behavior. *Dalton Trans.* **2021**, *50*, 15473–15487. [CrossRef]
9. Konieczny, P.; Sas, W.; Czernia, D.; Pacanowska, A.; Fitta, M. Magnetic cooling: A molecular perspective. *Dalton Trans.* **2022**, *51*, 12762–12780. [CrossRef] [PubMed]
10. Zhong, X.; Hu, J.-J.; Yao, S.-L.; Zhang, R.-J.; Wang, J.-J.; Cai, D.-G.; Luo, T.-K.; Peng, Y.; Liu, S.-J.; Wen, H.-R. Gd(III)-based inorganic polymers, metal-organic frameworks and coordination polymers for magnetic refrigeration. *CrystEngComm* **2022**, *24*, 2370–2382. [CrossRef]
11. Fan, C.H.; Bai, K.P.; Luo, Q.C.; Han, T.; Huang, C.; Zheng, Y.Z.; Chen, W.P. A new family of SO_4^{2-}-templated 3d-4f high-nuclearity clusters: Syntheses, structures, and magnetic properties. *Chin. J. Chem.* **2024**, *42*, 2438–2444. [CrossRef]
12. Liu, S.J.; Han, S.D.; Zhao, J.P.; Xu, J.L.; Bu, X.H. In-situ synthesis of molecular magnetorefrigerant materials. *Coord. Chem. Rev.* **2019**, *394*, 39–52. [CrossRef]
13. Liu, J.L.; Chen, Y.C.; Tong, M.L. Molecular design for cryogenic magnetic coolants. *Chem. Rec.* **2016**, *16*, 825–834. [CrossRef]
14. Han, S.D.; Miao, X.H.; Liu, S.J.; Bu, X.H. Magnetocaloric effect and slow magnetic relaxation in two dense (3,12)-connected lanthanide complexes. *Inorg. Chem. Front.* **2014**, *1*, 549–552. [CrossRef]
15. Zheng, X.Y.; Jiang, Y.H.; Zhuang, G.L.; Liu, D.P.; Liao, H.G.; Kong, X.J.; Long, L.S.; Zheng, L.S. A gigantic molecular wheel of $\{Gd_{140}\}$: A new member of the molecular wheel family. *J. Am. Chem. Soc.* **2017**, *139*, 18178–18181. [CrossRef]
16. Luo, X.M.; Hu, Z.B.; Lin, Q.F.; Cheng, W.W.; Cao, J.P.; Cui, C.H.; Mei, H.; Song, Y.; Xu, Y. Exploring the performance improvement of magnetocaloric effect based Gd-exclusive cluster Gd_{60}. *J. Am. Chem. Soc.* **2018**, *140*, 11219–11222. [CrossRef] [PubMed]
17. Zhitomirsky, M.E. Enhanced magnetocaloric effect in frustrated magnets. *Phys. Rev. B* **2003**, *67*, 1–7. [CrossRef]
18. Chang, L.X.; Xiong, G.; Wang, L.; Cheng, P.; Zhao, B. A 24-Gd nanocapsule with a large magnetocaloric effect. *Chem. Commun.* **2013**, *49*, 1055–1057. [CrossRef]
19. Ho, T.L. Hard soft acids bases (HSAB) principle and organic-chemistry. *Chem. Rev.* **1975**, *75*, 1–20. [CrossRef]
20. Zheng, X.Y.; Kong, X.J.; Zheng, Z.P.; Long, L.S.; Zheng, L.S. High-nuclearity lanthanide-containing clusters as potential molecular magnetic coolers. *Acc. Chem. Res.* **2018**, *51*, 517–525. [CrossRef]

21. Zheng, X.Y.; Xie, J.; Kong, X.J.; Long, L.S.; Zheng, L.S. Recent advances in the assembly of high-nuclearity lanthanide clusters. *Coord. Chem. Rev.* **2019**, *378*, 222–236. [CrossRef]
22. Iki, N.; Tanaka, T.; Hiro-oka, S.; Shinoda, K. Self-assembly of a trilanthanide(III) core sandwiched between two thiacalix[4] arene ligands. *Eur. J. Inorg. Chem.* **2016**, *2016*, 5020–5027. [CrossRef]
23. Tian, H.W.; Hong, J.Q.; Wang, K.; del Rosal, I.; Maron, L.; Zhou, X.G.; Zhang, L.X. Unprecedented reaction mode of phosphorus in phosphinidene rare-earth complexes: A joint experimental-theoretical study. *J. Am. Chem. Soc.* **2018**, *140*, 102–105. [CrossRef] [PubMed]
24. Li, Z.P.; Wang, D.; Zhou, Z.H.; Zhao, G.Y.; Li, Q.; Bi, Y.F.; Zheng, Z.P. Thiacalix[4]arene-sandwiched sandglass-like Ln_9 Clusters (Ln = Tb and Eu): Insights into the selective luminescence quenching properties by p-nitrobenzene derivatives. *Inorg. Chem.* **2022**, *61*, 20814–20823. [CrossRef] [PubMed]
25. Ying, J.; Gao, N.; Mou, H.C.; Tian, A.X. Rare earth mono-substituted Keggin dimmers: Structures, electrochemical, supercapacitor and magnetic properties. *J. Solid State Chem.* **2022**, *314*, 1–11. [CrossRef]
26. Ohama, K.; Komiya, M.; Yamatoya, T.; Sawamura, R.; Karashimada, R.; Gao, S.; Ozawa, Y.; Osada, K.; Aoki, I.; Nagasaki, T.; et al. Albumin nanoparticle electrostatically loaded with highly anionic Gd-thiacalixarene complex for MRI-guided neutron capture therapy. *Colloids Surf., A* **2024**, *699*, 1–13. [CrossRef]
27. Marin, R.; Gálico, D.A.; Gayfullina, R.; Moilanen, J.O.; Carlos, L.D.; Jaque, D.; Murugesu, M. A zero-field single-molecule magnet with luminescence thermometry capabilities containing soft donors. *J. Mater. Chem. C* **2022**, *10*, 13946–13953. [CrossRef]
28. Chen, S.M.; Xiong, J.; Zhang, Y.Q.; Yuan, Q.; Wang, B.W.; Gao, S. A soft phosphorus atom to "harden" an erbium(III) single-ion magnet. *Chem. Sci.* **2018**, *9*, 7540–7545. [CrossRef]
29. Liu, S.S.; Lang, K.; Zhang, Y.Q.; Yang, Q.; Wang, B.W.; Gao, S. A distinct magnetic anisotropy enhancement in mononuclear dysprosium-sulfur complexes by controlling the Dy-ligand bond length. *Dalton Trans.* **2016**, *45*, 8149–8153. [CrossRef]
30. Canaj, A.B.; Dey, S.; Céspedes, O.; Wilson, C.; Rajaraman, G.; Murrie, M. There is nothing wrong with being soft: Using sulfur ligands to increase axiality in a Dy(III) single-ion magnet. *Chem. Commun.* **2020**, *56*, 1533–1536. [CrossRef] [PubMed]
31. Tziotzi, T.G.; Gracia, D.; Dalgarno, S.J.; Schnack, J.; Evangelisti, M.; Brechin, E.K.; Milios, C.J. A $\{Gd_{12}Na_6\}$ molecular quadruple-wheel with a record magnetocaloric effect at low magnetic fields and temperatures. *J. Am. Chem. Soc.* **2023**, *145*, 7743–7747. [CrossRef]
32. Braun, J.; Seufert, D.; Anson, C.E.; Tang, J.K.; Powell, A.K. An effectively uncoupled Gd_8 cluster formed through fixation of atmospheric CO_2 showing excellent magnetocaloric properties. *Int. J. Mol. Sci* **2024**, *25*, 264. [CrossRef]
33. Wang, Y.F.; Wang, Y.X.; Yang, Q.Q.; Yin, B. Auxiliary rather than dominant. the role of direct Dy-S coordination in single-molecule magnet unveiled via ab initio study. *J. Phys. Chem. A* **2024**, *128*, 5285–5297. [CrossRef]
34. Kumari, N.; Jassal, M.; Agrawal, A.K. Effect of metal ion on UV protective and antimicrobial properties of in-situ synthesized pyrithione complexes on cellulosic textiles. *Mater. Today Commun.* **2023**, *34*, 1–13. [CrossRef]
35. Han, T.; Wang, X.Q.; Guo, T.; Cao, H.S.; Chen, W.P.; He, L. Modulation of the magnetic dynamics in two air-stable sulfur-ligated dysprosium complexes via polymerization. *Dalton Trans.* **2023**, *52*, 7551–7557. [CrossRef]
36. Yuan, F.; Li, T.; Zhang, M.; Qian, H. Synthesis and crystal structure of tri(pyrithione) cerium complex and its catalytic property for oxidation of benzoin to benzil. *Synth. React. Inorg. Met.-Org. Nano-Met. Chem.* **2013**, *43*, 1510–1513. [CrossRef]
37. Niu, D.Z.; Mu, L.L.; Lu, Z.S.; Song, B.L.; Sun, B.W. Synthesis and crystal structure of $Pr_3(DMSO)_2$ (Hmpo=2-mercaptopyridine N-oxide). *J. Chem. Crystallogr.* **2004**, *34*, 195–198. [CrossRef]
38. Xiong, R.G.; Zuo, J.L.; You, X.Z.; Huang, X.Y. Synthesis and X-ray structure of the first lanthanide 2-mercaptopyridine N-oxide complex, tris-(1-hydroxy-2(1H)-pyridinethionato-O,S) bis sulfinylbis(methane) samarium(III). *Polyhedron* **1996**, *15*, 3321–3324. [CrossRef]
39. Hu, Y.H.; Weng, L.H.; Huang, L.G.; Chen, X.T.; Wu, D.X.; Kang, B.S. Structure of tris(2-mercaptopyridine 1-oxido)cobalt(III) acetonitrile solvate. *Acta Crystallogr. Sect. C Cryst. Struct. Commun.* **1991**, *47*, 2655–2656. [CrossRef]
40. West, D.X.; Frank, C.A. 2 series of rare-earth complexes of the 2-thiopyridine N-oxide anion. *J. Inorg. Nucl. Chem.* **1979**, *41*, 49–53. [CrossRef]
41. Wang, T.; Wang, H.; Sun, W. Sandglass-like Ln_9 nanoclusters with magnetocaloric effect and lanthanide-centered luminescence. *Cryst. Growth Des.* **2024**, *24*, 8076–8084. [CrossRef]
42. Pandey, P.; Chauhan, D.; Walawalkar, M.G.; Gupta, S.K.; Meyer, F.; Rajaraman, G.; Murugavel, R. Hourglass-shaped homo- and heteronuclear nonanuclear lanthanide clusters: Structures, magnetism, photoluminescence, and theoretical analysis. *Inorg. Chem.* **2024**, *63*, 11963–11976. [CrossRef]
43. Hu, P.; Li, S.H.; Cao, L.H.; Liu, A.G.; Zhuang, G.L.; Ji, L.D.; Li, B. Construction of a high nuclear gadolinium cluster with enhanced magnetocaloric effect through structural transition. *Acs Omega* **2022**, *7*, 38782–38788. [CrossRef]
44. Casanova, D.; Cirera, J.; Llunell, M.; Alemany, P.; Avnir, D.; Alvarez, S. Minimal distortion pathways in polyhedral rearrangements. *J. Am. Chem. Soc.* **2004**, *126*, 1755–1763. [CrossRef]

45. Panguluri, S.P.K.; Jourdain, E.; Chakraborty, P.; Klyatskaya, S.; Kappes, M.M.; Nonat, A.M.; Charbonnière, L.J.; Ruben, M. Yb-to-Eu cooperative sensitization upconversion in a multifunctional molecular nonanuclear lanthanide cluster in solution. *J. Am. Chem. Soc.* **2024**, *146*, 13083–13092. [CrossRef] [PubMed]
46. Knighton, R.C.; Soro, L.K.; Lecointre, A.; Pilet, G.; Fateeva, A.; Pontille, L.; Francés-Soriano, L.; Hildebrandt, N.; Charbonnière, L.J. Upconversion in molecular hetero-nonanuclear lanthanide complexes in solution. *Chem. Commun.* **2021**, *57*, 53–56. [CrossRef] [PubMed]
47. Hu, P.; Cao, L.H.; Liu, A.G.; Zhang, Y.Q.; Zhang, T.L.; Li, B. Modulating the relaxation dynamics via structural transition from a dinuclear dysprosium cluster to a nonanuclear cluster. *Dalton Trans.* **2021**, *50*, 12814–12820. [CrossRef] [PubMed]
48. Huang, Y.; Qin, Y.R.; Ge, Y.; Cui, Y.F.; Zhang, X.M.; Li, Y.H.; Yao, J.L. Rationally assembled nonanuclear lanthanide clusters: Dy_9 displays slow relaxation of magnetization and Tb_9 serves as luminescent sensor for Fe^{3+}, CrO_4^{2-} and $Cr_2O_7^{2-}$. *New J. Chem.* **2019**, *43*, 19344–19354. [CrossRef]
49. Griffiths, K.; Kühne, I.A.; Tizzard, G.J.; Coles, S.J.; Kostakis, G.E.; Powell, A.K. Twists to the spin structure of the Ln_9-diabolo motif exemplified in two $\{Zn_2Ln_2\}Ln_9\{Zn_2\}$ coordination clusters. *Inorg. Chem.* **2019**, *58*, 2483–2490. [CrossRef]
50. Wang, H.S.; Long, Q.Q.; Yin, C.L.; Xu, Z.W.; Pan, Z.Q. Syntheses, crystal structures and magnetic properties of sandglass Dy_9^{III} and irregular tetrahedron Dy_4^{III} complexes. *Polyhedron* **2018**, *141*, 69–76. [CrossRef]
51. Chen, H.F.; Yang, X.P.; Jiang, D.M.; Shi, D.L.; Zhang, L.J. Construction of NIR luminescent polynuclear lanthanide-based nanoclusters with sensing properties towards metal ions. *Dalton Trans.* **2018**, *47*, 13880–13886. [CrossRef]
52. Zheng, X.Y.; Peng, J.B.; Livera, M.; Luo, Y.; Wang, Y.Y.; Kong, X.J.; Long, L.S.; Zheng, Z.P.; Zheng, L.S. Selective formation of chromogen I from N-acetyl-D-glucosamine upon lanthanide coordination. *Inorg. Chem.* **2017**, *56*, 110–113. [CrossRef]
53. Mylonas-Margaritis, I.; Kitos, A.A.; Panteli, C.C.; Skordi, K.; Tasiopoulos, A.J.; Bekiari, V.; Escuer, A.; Perlepes, S.P. 2-hydroxybenzophenone-controlled self-assembly of enneanuclear lanthanide(III) hydroxo coordination clusters with an "hourglass"-like topology. *Inorg. Chem. Commun.* **2017**, *83*, 118–122. [CrossRef]
54. Omagari, S.; Nakanishi, T.; Kitagawa, Y.; Seki, T.; Fushimi, K.; Ito, H.; Meijerink, A.; Hasegawa, Y. Critical role of energy transfer between terbium ions for suppression of back energy transfer in nonanuclear terbium clusters. *Sci. Rep.* **2016**, *6*, 1–11. [CrossRef] [PubMed]
55. Greisch, J.F.; Chmela, J.; Harding, M.E.; Klopper, W.; Kappes, M.M.; Schooss, D. Gas-phase photoluminescence characterization of stoichiometrically pure nonanuclear lanthanoid hydroxo complexes comprising europium or gadolinium. *Inorg. Chem.* **2016**, *55*, 3316–3323. [CrossRef] [PubMed]
56. Zou, H.H.; Sheng, L.B.; Chen, Z.L.; Liang, F.P. Lanthanide nonanuclear clusters with sandglass-like topology and the SMM behavior of dysprosium analogue. *Polyhedron* **2015**, *88*, 110–115. [CrossRef]
57. Omagari, S.; Nakanishi, T.; Seki, T.; Kitagawa, Y.; Takahata, Y.; Fushimi, K.; Ito, H.; Hasegawa, Y. Effective photosensitized energy transfer of nonanuclear terbium clusters using methyl salicylate derivatives. *J. Phys. Chem. A* **2015**, *119*, 1943–1947. [CrossRef]
58. Nakanishi, T.; Suzuki, Y.; Doi, Y.; Seki, T.; Koizumi, H.; Fushimi, K.; Fujita, K.; Hinatsu, Y.; Ito, H.; Tanaka, K.; et al. Enhancement of optical faraday effect of nonanuclear Tb(III) complexes. *Inorg. Chem.* **2014**, *53*, 7635–7641. [CrossRef]
59. Greisch, J.F.; Harding, M.E.; Schäfer, B.; Ruben, M.; Klopper, W.; Kappes, M.M.; Schooss, D. Characterization of nonanuclear europium and gadolinium complexes by gas-phase luminescence spectroscopy. *J. Phys. Chem. Lett.* **2014**, *5*, 1727–1731. [CrossRef]
60. Zhang, B.; Xiao, T.; Liu, C.M.; Li, Q.; Zhu, Y.Y.; Tang, M.S.; Du, C.X.; Song, M.P. Systematic study of the luminescent europium-based nonanuclear clusters with modified 2-hydroxybenzophenone ligands. *Inorg. Chem.* **2013**, *52*, 13332–13340. [CrossRef]
61. Singh-Wilmot, M.A.; Sinclair, R.A.; Andrews, M.; Rowland, C.; Cahill, C.L.; Murugesu, M. Nonanuclear lanthanide(III) nanoclusters: Structure, luminescence and magnetic properties. *Polyhedron* **2013**, *53*, 187–192. [CrossRef]
62. Xu, X.B.; Zhao, L.; Xu, G.F.; Guo, Y.N.; Tang, J.K.; Liu, Z.L. A diabolo-shaped Dy_9 cluster: Synthesis, crystal structure and magnetic properties. *Dalton Trans.* **2011**, *40*, 6440–6444. [CrossRef]
63. Alexandropoulos, D.I.; Mukherjee, S.; Papatriantafyllopoulou, C.; Raptopoulou, C.P.; Psycharis, V.; Bekiari, V.; Christou, G.; Stamatatos, T.C. A new family of nonanuclear lanthanide clusters displaying magnetic and optical properties. *Inorg. Chem.* **2011**, *50*, 11276–11278. [CrossRef] [PubMed]
64. Baril-Robert, F.; Petit, S.; Pilet, G.; Chastanet, G.; Reber, C.; Luneau, D. Site-selective lanthanide doping in a nonanuclear yttrium(III) cluster revealed by crystal structures and luminescence spectra. *Inorg. Chem.* **2010**, *49*, 10970–10976. [CrossRef]
65. Petit, S.; Baril-Robert, F.; Pilet, G.; Reber, C.; Luneau, D. Luminescence spectroscopy of europium(III) and terbium(III) penta-, octa- and nonanuclear clusters with β-diketonate ligands. *Dalton Trans.* **2009**, 6809–6815. [CrossRef] [PubMed]
66. Volpe, M.; Bombieri, G.; Clemente, D.A.; Foresti, E.; Grillone, M.D. Synthesis and physico-chemical characterization of a new series of hydroxide ion acetylacetonate lanthanide(III)-ditungsten decacarbonyl hydride complexes. *J. Alloys Compd.* **2004**, *374*, 382–386. [CrossRef]
67. Addamo, M.; Bombieri, G.; Foresti, E.; Grillone, M.D.; Volpe, M. Assembling process of charged nonanuclear cationic lanthanide(III) clusters assisted by dichromium decacarbonyl hydride. *Inorg. Chem.* **2004**, *43*, 1603–1605. [CrossRef]

68. Xu, G.; Wang, Z.M.; He, Z.; Lu, Z.; Liao, C.S.; Yan, C.H. Synthesis and structural characterization of nonanuclear lanthanide complexes. *Inorg. Chem.* **2002**, *41*, 6802–6807. [CrossRef]
69. Hubert-Pfalzgraf, L.G.; Miele-Pajot, N.; Papiernik, R.; Vaissermann, J. A novel example of self-assembly in lanthanide chemistry: Synthesis and molecular structure of $Na(EtOH)_6Y_9(\mu_4\text{-}O)_2(\mu_3\text{-}OH)_8\{\mu\text{-}\eta^2\text{-}MeC(O)CHC(O)OEt\}_8\{\eta^2\text{-}MeC(O)CHC(O)OEt\}_8$. *J. Chem. Soc. Dalton Trans.* **1999**, 4127–4130. [CrossRef]
70. Chilton, N.F.; Anderson, R.P.; Turner, L.D.; Soncini, A.; Murray, K.S. PHI: A powerful new program for the analysis of anisotropic monomeric and exchange-coupled polynuclear d- and f-block complexes. *J. Comput. Chem.* **2013**, *34*, 1164–1175. [CrossRef]
71. Singh, M.K.; Rajeshkumar, T.; Kumar, R.; Singh, S.K.; Rajaraman, G. Role of (1,3) {Cu-Cu} interaction on the magneto-caloric effect of trinuclear $\{Cu^{II}\text{-}Gd^{III}\text{-}Cu^{II}\}$ complexes: Combined DFT and experimental studies. *Inorg. Chem.* **2018**, *57*, 1846–1858. [CrossRef] [PubMed]
72. Rajeshkumar, T.; Singh, S.K.; Rajaraman, G. A computational perspective on magnetic coupling, magneto-structural correlations and magneto-caloric effect of a ferromagnetically coupled $\{Gd^{III}\text{-}Gd^{III}\}$ pair. *Polyhedron* **2013**, *52*, 1299–1305. [CrossRef]

Disclaimer/Publisher's Note: The statements, opinions and data contained in all publications are solely those of the individual author(s) and contributor(s) and not of MDPI and/or the editor(s). MDPI and/or the editor(s) disclaim responsibility for any injury to people or property resulting from any ideas, methods, instructions or products referred to in the content.